Velocity variations in the uppermost mantle beneath the southern Sierra Nevada and Walker Lane

Brian Savage, Chen Ji, and Don V. Helmberger
Seismological Laboratory, California Institute of Technology, Pasadena, California, USA

Received 26 September 2001; revised 12 February 2002; accepted 5 March 2003; published 2 July 2003.

[1] We model *Pn* waveforms from two earthquakes in the southwestern United States (Mammoth Lakes, California, and western Nevada) to determine a velocity model of the crustal and mantle structure beneath the southern Sierra Nevada and Walker Lane. We derive a one-dimensional velocity model that includes a smooth crust-mantle transition east of Death Valley and extending south into the eastern Mojave desert. West of Death Valley and toward the Sierra Nevada a low-velocity mantle (V_p = 7.6 km/s) directly below the crust indicates the lithosphere is absent. At the base of this low-velocity structure (at 75–100 km depth) the *P* wave velocity jumps discontinuously to V_p 8.0 km/s. The area of low velocity is bounded by the Garlock Fault to the south and the Sierra Nevada to the west, but we cannot resolve its northern extent. However, on the basis of teleseismic travel times we postulate that the anomaly terminates at about 38°N. The presence of a low-velocity, upper mantle anomaly in this area agrees with geochemical research on xenoliths from the southern Sierras and recent studies of receiver functions, refraction profiles, tomography, and gravity. However, the velocity discontinuity at 75–100 km is a new discovery and may represent the top of the once present, now unaccounted for and possibly sunken Sierra Nevada lithosphere. *INDEX TERMS:* 7203 Seismology: Body wave propagation; 7205 Seismology: Continental crust (1242); 7218 Seismology: Lithosphere and upper mantle; 7260 Seismology: Theory and modeling; *KEYWORDS:* Sierra Nevada, lithosphere, mantle, crust, waveform, seismology

Citation: Savage, B., C. Ji, and D. V. Helmberger, Velocity variations in the uppermost mantle beneath the southern Sierra Nevada and Walker Lane, *J. Geophys. Res.*, *108*(B7), 2325, doi:10.1029/2001JB001393, 2003.

1. Introduction

[2] The Basin and Range province in western North America is bounded on the west by north-south trending deep valleys and mountain ranges consisting of California's Central Valley, the Sierra Nevada, and Walker Lane (Figure 1). Walker Lane includes Death Valley and Owens Valley and trends parallel to the Sierra Nevada from the Garlock fault in the south to central Oregon. The Sierra Nevada transitions from sloping foothills in the west to over 4 km of abrupt relief in the east. This dramatic topography in the Sierra Nevada and Walker Lane is a result of the complex tectonic evolution during the Cenozoic (65 Ma to present) [*Bateman and Eaton*, 1967; *Dumitru et al.*, 1991; *Wernicke*, 1992; *Burchfiel et al.*, 1992a, 1992b]. *Wernicke and Snow* [1998] use geologic reconstructions to suggest that prior to 8 Ma, the Sierra Nevada and California's Central Valley were moving west at >20 mm/yr relative to the Colorado Plateau. Kinematic models [*Wernicke and Snow*, 1998; *Snow and Wernicke*, 2000] suggest that from 8 Ma to present the Sierra Nevada began moving at 15 mm/yr to the northwest to north-northwest. At the same time (~20 Ma), Sierra Nevada uplift began, and the slab window due to the passing Farallon Plate formed [*Atwater and Stock*, 1998]. The mechanism of Sierra Nevada uplift is still under debate, and the kinematics of the surrounding region are still poorly understood.

[3] Geophysical and geochemical studies provide important data which constrain the structural properties of the Sierra Nevada and allow us to assess models of their uplift. Reduced heat flow in the Sierra Nevada [*Saltus and Lachenbruch*, 1991] suggests a lateral increase in heat flux at the base of the crust and large thermal gradients in the lithosphere beneath the eastern slope of the Sierra Nevada toward the Basin and Range. Geochemical data from *Ducea and Saleeby* [1996, 1998a, 1998b, 1998c] show a corresponding rapid structural change in the lithosphere and upper mantle. Examination of xenoliths [*Ducea and Saleeby*, 1998c] shows that prior to 6 Ma, the Sierra Nevada was underlain by an ultramafic, eclogitic root or mantle lithosphere. At ~6 Ma the deep (~75 km), eclogitic lithosphere transformed by an unknown mechanism into hot, asthenospheric-like mantle. Gravity modeling by *Fliedner and Ruppert* [1996] suggests lateral density variations in the upper mantle, in agreement with heat flow and xenolith data that imply that a hotter, less dense, asthenospheric mantle on the eastern edge of the Sierra Nevada extends into the Basin and Range.

[4] Dynamic models of western North American that include subduction, uplift of the Sierra Nevada, and extension of the Basin and Range do not exist at present. However, smaller-scale investigations of the relative effects

0148-0227/03/2001JB001393$09.00

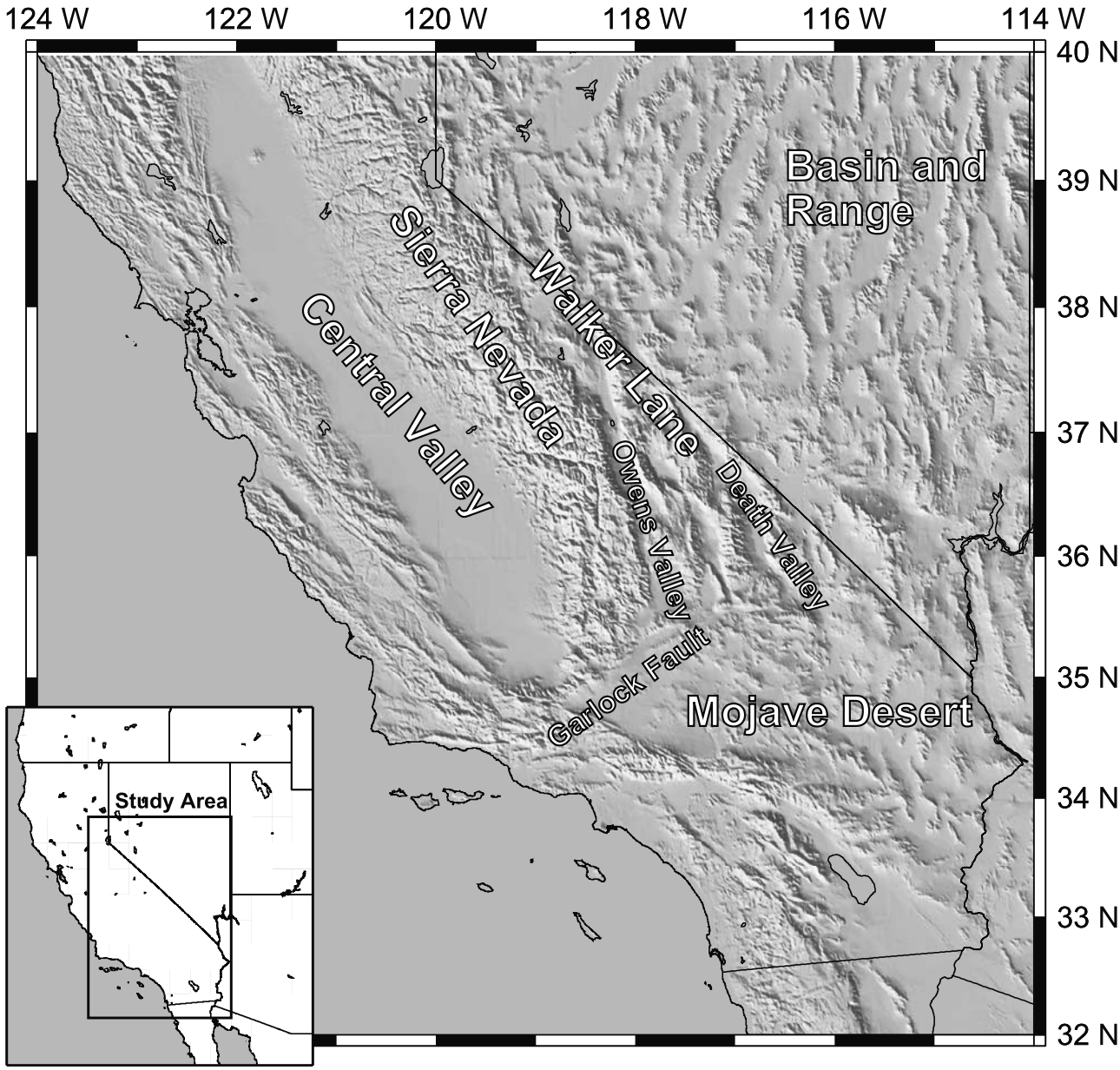

Figure 1. Map of California and Nevada within western North America showing relevant provinces and their locale relative to one another. A complex, yet poorly understood, series of tectonic events occurred to produce the topography across the region. The area within the Sierra Nevada and Walker Lane south of 38°N is the focus of this study.

of plate boundary forces, lithosphere basal forces, and buoyancy forces [see *Sonder and Jones*, 1999, Table 1; *Chase and Wallace*, 1988; *Zandt and Carrigan*, 1993; *Liu and Zandt*, 1996] may guide broader-scale studies in the future. In this study we do not attempt to discern which forces are dominant in the system, but we aim to place constraints on the structural properties of the upper mantle and lower crust with high-quality seismic waveform data.

2. Geophysical Observations

[5] While an investigation of the entire Sierra Nevada range and Walker Lane from north to south would be desirable, the lack of available waveform data in the north limits our study area to the southern region. However, teleseismic *P*, *S*, and *ScS* waves [*Ding and Helmberger*, 1997; *Melbourne and Helmberger*, 2001] from earthquakes in South America propagate faster when they travel through the Sierra Nevada north of 38°N than those that propagate through the southern Sierra Nevada, indicating a contrast from north to south.

[6] Using a small set of gravity data and seismic travel times, *Lawson* [1936] and *Byerly* [1937] suggest that the Sierra Nevada is in isostatic equilibrium with a thick crustal root. Deployments of seismic refraction lines parallel and perpendicular to the Sierra Nevada axis have estimated the vertical extent of the crustal root. Figure 2 shows the

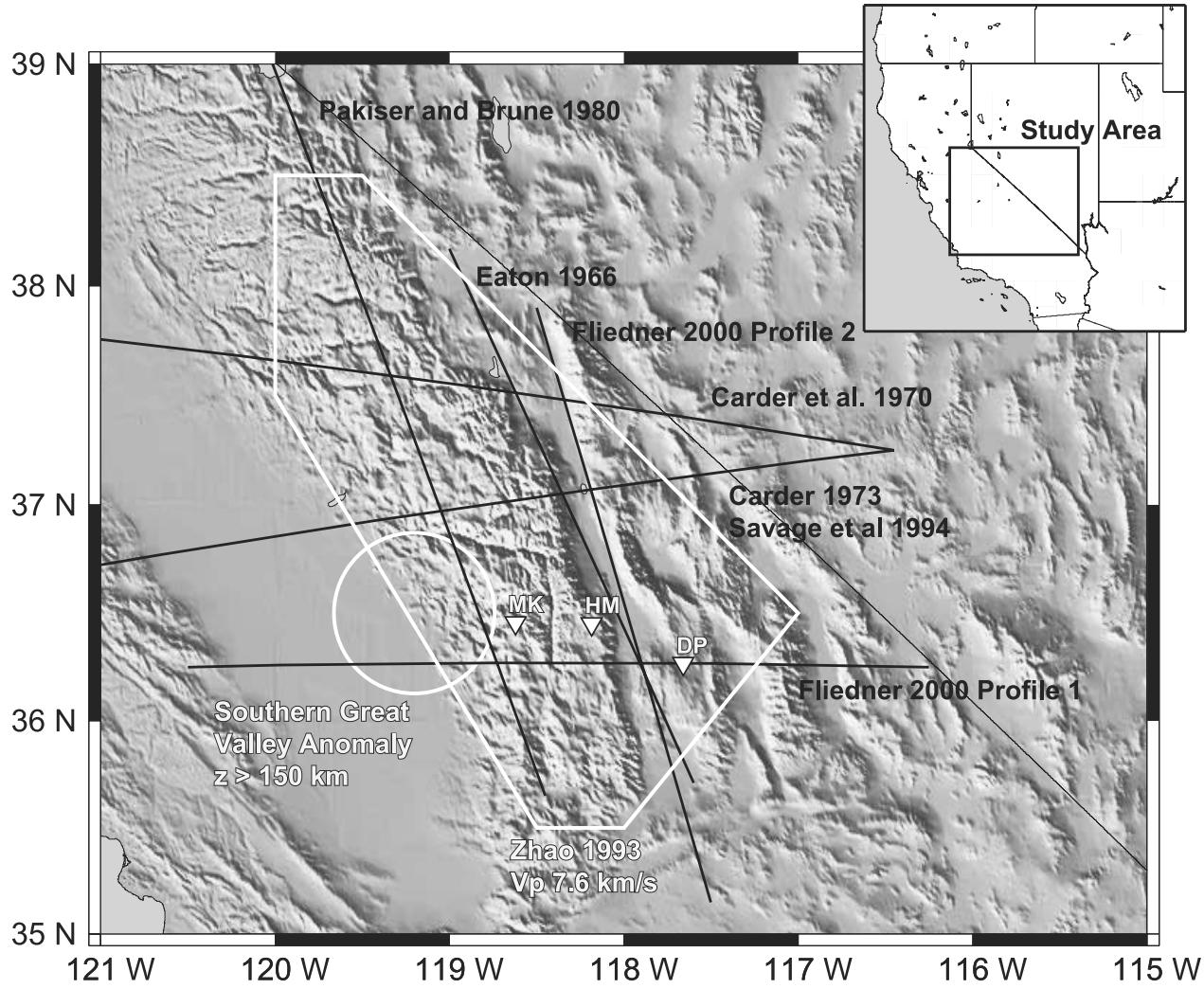

Figure 2. Regional map of the southern Sierra Nevada and Walker Lane showing previous passive and active experiments. All black lines and labels refer to active source studies with the lines representing the refraction profiles. Each line label pair is unique except for *Carder* [1973] and *Savage et al.* [1994], which share the same profile. White features show passive experiments. The southern Great Valley Anomaly (circle) [*Biasi and Humphreys*, 1992] is a region of high velocity at a depth of ~150 km. The inverted triangles [*Jones and Phinney*, 1998] are temporary seismic stations used to compute receiver functions, and the large white area which encloses the entire southern Sierra Nevada is a region of 7.6 km/s *Pn* velocity from the tomography of *Zhao* [1993].

location of different active source refraction experiments in and around the Sierra Nevada.

[7] Each refraction experiment reports late *Pn* arrivals along paths crossing the Sierra Nevada mountains that indicate that there is either a thick crustal root or a low-velocity mantle. However, the reported velocity structure is dependent on orientation of the refraction profile across the Sierra Nevada.

[8] Refraction lines parallel to the Sierra Nevada [*Eaton*, 1966; *Pakiser and Brune*, 1980] relate the delayed *Pn* travel times to a crustal root, in agreement with previous gravity studies [*Lawson*, 1936]. Models invoking crustal roots exceeding 50 km and velocities in the lower crust of 6.9 km/s explain the travel times of both studies [*Eaton*, 1966; *Pakiser and Brune*, 1980]. Rayleigh wave phase velocities measured by *Crough and Thompson* [1977] along a similar profile show a low-velocity mantle beneath a thick Sierra Nevada crust and the Basin and Range. Their results are also based upon previous work by *Eaton* [1966]. In contrast, perpendicular profiles [*Carder et al.*, 1970; *Carder*, 1973; *Savage et al.*, 1994] interpret the late *Pn* travel times as a result of a low V_p mantle and a crustal thickness of ~35 km thickness. *Savage et al.* [1994] suggest a V_p anomaly of 7.2 km/s in the west to 7.7 km/s in the east.

[9] Recent seismic reflections and refractions both parallel and perpendicular to the Sierra Nevada, in conjunction with gravity modeling, receiver functions, and teleseismic arrival times [*Wernicke et al.*, 1996; *Jones et al.*, 1994; *Jones and Phinney*, 1998; *Fliedner et al.*, 2000], argue

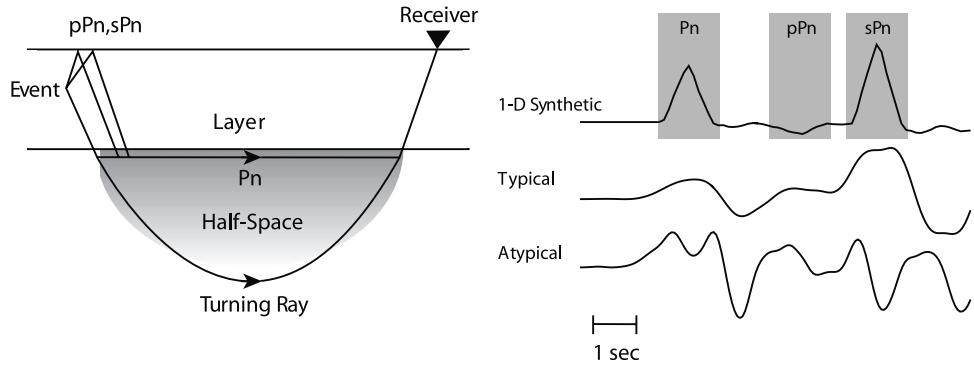

Figure 3. (left) Ray paths for *Pn*, *pPn*, and *sPn* for a model of a layer over a half-space (simplification of the crust over the mantle). *Pn* is normally thought of as an arrival whose path is directly along the interface between the layer and half-space. However, the energy which creates the *Pn* arrival is distributed across a large depth range within the half-space, as indicated by the gray shading. Eventually, at large epicentral distance, *Pn* merges with the turning ray in a half-space. (right) Vertical velocity waveforms (top) including *Pn*, *pPn*, and *sPn* for the layer over a half-space velocity model (left) (450 km). Notice how the typical data are similar to the simple model at the top, in contrast to the complicated, abnormal waveform.

against the existence of a thick crustal root. In particular, *Jones and Phinney* [1998] use a suite of receiver functions to identify a low-velocity zone within the crust and the presence of a low-velocity mantle below the Sierra Nevada, shown as inverted triangles in Figure 2. Upper mantle tomographic studies of the area [*York and Helmberger*, 1973; *Biasi and Humphreys*, 1992; *Zhao*, 1993; *Pollitz*, 1999] also support a lower-velocity mantle beneath much of the southern Sierra Nevada and Walker Lane (white outline in Figure 2). To complement recent studies in tomography, gravity, and receiver functions, the advent of dense, large-scale broadband seismic arrays provides travel times and waveform data particularly suited to image the crust and upper mantle.

3. Data

[10] We use two types of data to illuminate the crust-mantle interface beneath the southern Sierra Nevada and Walker Lane. First, using a small set of travel time data from an event in northern California, we infer a dramatic velocity structure within the study region. Second, we model waveform data from earthquakes in Mammoth Lakes and near the California-Nevada border to constrain the velocity structure of the crust-mantle interface within the study area.

[11] Both data sets feature *Pn* arrivals, including *pPn* and *sPn*. To illustrate how the *Pn* arrivals sample the crust-mantle interface, synthetics for a simple model of a layer over a half-space are shown in Figure 3. *Pn* is a refracted phase which propagates in the mantle just below the crust. The shaded region in Figure 3 indicates the sampling region of *Pn*. Generally, the greater the epicentral distance, the greater the penetration of *Pn* below the Moho. The depth phases, *pPn* and *sPn*, arrive later than *Pn* as they first travel to the surface as either upgoing *P* or *S* waves before traversing the same path as *Pn* below the Moho. The relative arrival time of *Pn*, *pPn*, and *sPn* is controlled by the depth of the event. The wave shape of *Pn*, as in Figure 3, is an integration of the far-field ground motion, $S(t)$. If we assume that the shape of $S(t)$ is a triangle in displacement, then *Pn* signals are shaped like ramps:

$$P_n(t)_{\text{Displacement}} \cong \int S(t)dt. \tag{1}$$

After differentiating, the ramp in displacement changes into a triangular function in velocity:

$$P_n(t)_{\text{Velocity}} \cong \frac{d}{dt}\int S(t)dt = S(t). \tag{2}$$

In contrast, ground motion velocities from postcritical reflections such as *PmP* (not shown) will appear "double-sided", that is, has a positive triangular pulse followed by a negative one. Also included in Figure 3 is the portion of the synthetics used for comparison with the data. Comparing the simple one-dimensional (1-D) model and the "typical" waveform shows that both are composed of simple, triangular-shaped *Pn* and *sPn* arrivals. The "atypical" trace is complex because the existence of a second pulse is followed by a large downswing occurring near the *Pn* arrival.

3.1. Travel Times

[12] We show *Pn* travel time data from an earthquake in Santa Rosa, northern California, in Figure 4a, while selected waveform data from the same earthquake are displayed in Figure 4b with a 8.0 km/s reduction velocity. Both data types highlight interesting features around the Sierra Nevada. In Figure 4a, blue to white stations record relatively short *Pn* travel times corresponding to a *Pn* velocity of ~7.8–8.0 km/s, while white to red stations record larger delays and slower *Pn* velocities (~7.6–7.8 km/s). *Pn* waves that travel parallel to the San Andreas Fault and do not traverse the Sierra Nevada or Walker Lane regions have

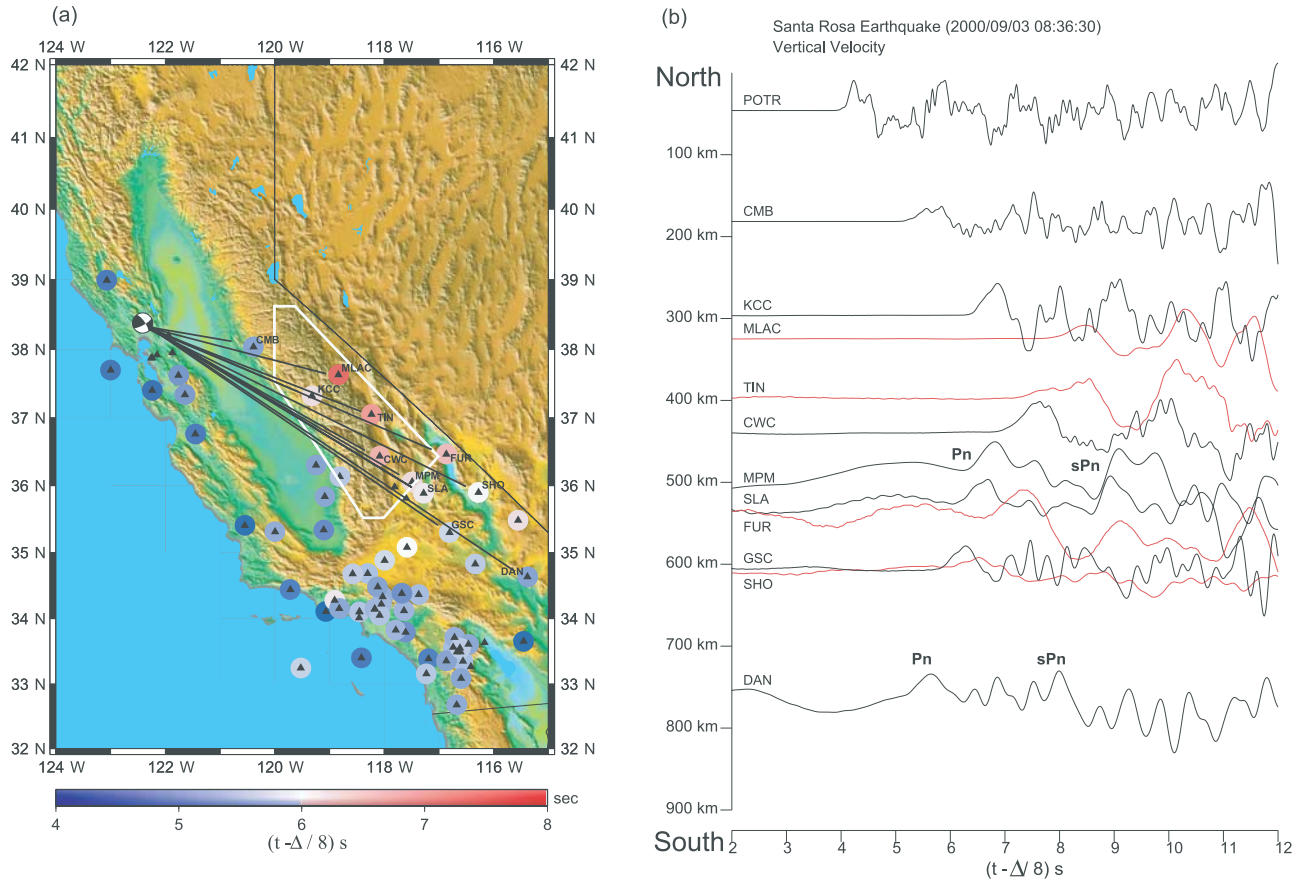

Figure 4. (a) *Pn* arrival times with the color indicating the delay with respect to an arrival of 8.0 km/s. The earthquake, location indicated by the source mechanism, is located in Santa Rosa in northern California. Ray paths are shown for selected stations, and Figure 4b shows the corresponding waveforms. (b) Vertical velocity data from the same earthquake as in Figure 4a. Notice the clustering of late *Pn* times, white to red, for paths which cross the Sierra Nevada. Stations farther to the east show a much more pronounced slowing compared with those to the west. Those stations to the northeast, marked in red, are also longer period than those just slightly to the southwest, black. The white outline was determined by *Zhao* [1993] to be slower than average mantle, 7.6 km/s, using regional *Pn* travel times.

similar, short travel times, as shown by the cluster of blue circles near Los Angeles. *Pn* recorded in the Sierra Nevada and Walker Lane have longer travel times (white to red circles) with a maximum at station MLAC (Mammoth Lakes, California). Great circle paths for these slower arrivals are shown in Figure 4a as solid lines. About 1 s of the delay at MLAC is probably the result of a large magma chamber beneath the area [*Bailey et al.*, 1976; *Weiland et al.*, 1995]. Stations farther to the southeast also indicate late first arrivals.

[13] The seismic waveform data (Figure 4b) with station labels show that *Pn* recorded to the north (red waveforms) arrive later and have longer-period waveforms than the impulsive, earlier arrivals recorded to the south (black waveforms). The waveform data and travel time differences suggest complex structure within the southern Sierra Nevada and Walker Lane. These data support a very sharp transition from KCC to MLAC (apparent mantle $V_p < 6$ km/s) and then a gradual increase in velocity, up to 8.0 km/s, toward the southeast. We did not attempt to explain these data in detail as it would require 3-D modeling because the ray paths sample distinctly different regions.

3.2. Waveforms

[14] *Pn* waveforms from two mid-1999 earthquakes that occurred in Mammoth Lakes and western Nevada (Figure 5) provide extensive coverage that can help map out the crust-mantle interface beneath the southern Sierra Nevada and Walker Lane. These waveforms data were recorded by broadband instruments of TriNet. Instrument responses were deconvolved from the data to obtain ground motion velocity. The data are low-pass filtered at 1.5 Hz and plotted as a velocity time series, except where noted. Since we are modeling *Pn* and depth phases of *Pn*, which only arrive on the vertical and radial components and the vertical component of *Pn* is nearly identical to the radial component of *Pn*, we only consider the vertical component of the data.

[15] Tables 1 and 2 contain several estimates of source parameters for each earthquake. While the methods of source parameter determination are quite different, they

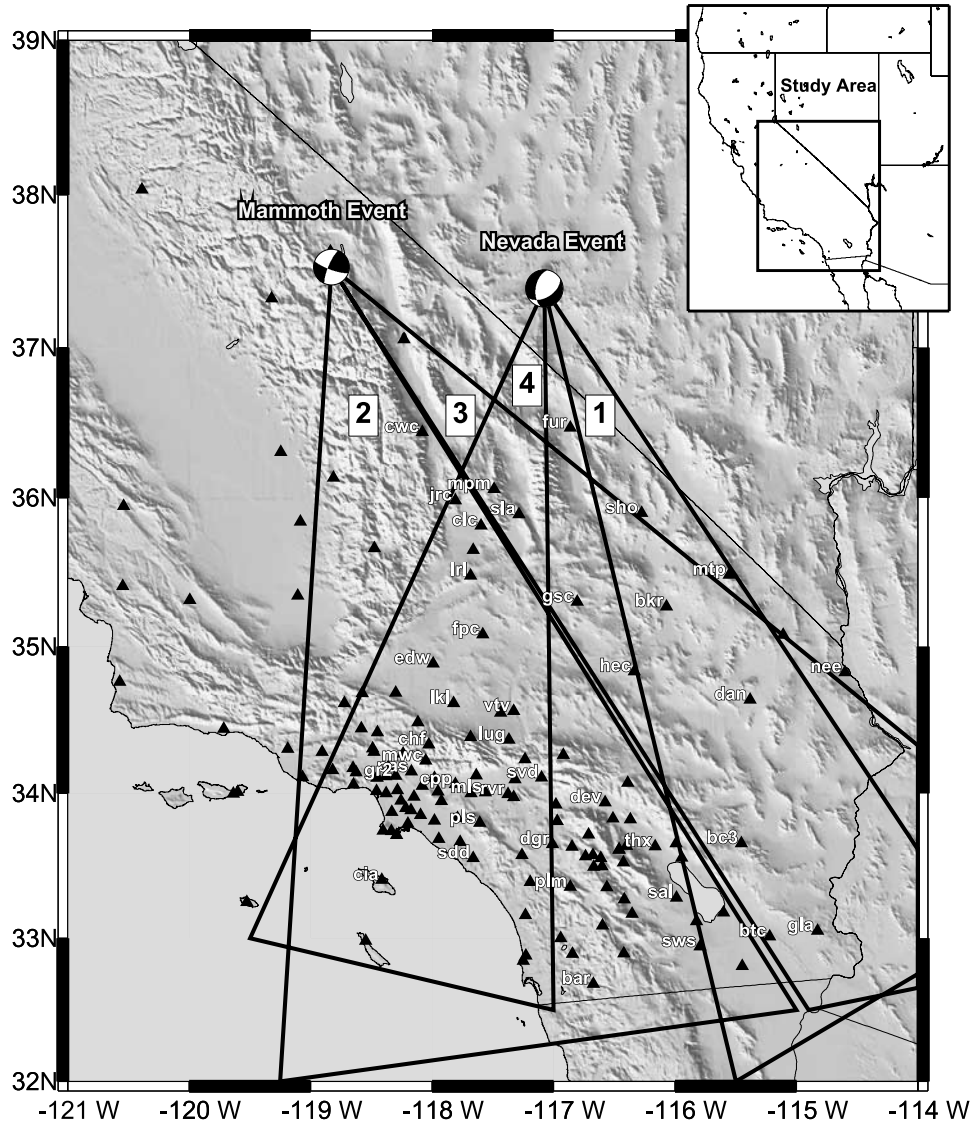

Figure 5. Map of California and Nevada, showing TriNet and Berkeley Digital Seismic Network (BDSN) stations as triangles, the source mechanisms used for this study, and the triangular swaths modeled using *Pn* waveforms. Studied triangular swaths are marked 1–4. Swaths 1 and 2 are used in waveform modeling, while swaths 3 and 4 are used only in model validation.

provide consistent results. We use the time domain moment tensor [*Pasyanos et al.*, 1996] solution for the earthquake in Mammoth Lakes and our independently determined solution for the earthquake near the California-Nevada border. The range of faulting parameters given for our independently determined solution represents a set of parameters in which no appreciable change is seen between the waveform data and synthetics. Source time functions are determined from the widths of direct *P* waves at short distances for each event. Triangles with a half width of 1 s are convolved with the point source synthetics to facilitate comparison with data.

Table 1. Mammoth, California (37.5298, −118.8172) 15 May 1999 (135) 1322:19.066 UT

Moment, dyn cm	Depth, km	Strike, deg	Dip, deg	Rake, deg	Source
4.30×10^{24} ($5.7M_w$)	8	203/110	79/77	13/169	SWPA[a]
2.31×10^{24} ($5.5M_w$)	8	203/294	85/80	−11/−174	TDMT[b]

[a]Surface wave phase analysis, University of California, Berkeley.
[b]Time domain moment tensor, University of California, Berkeley.

Table 2. California-Nevada Border (37.3887, −117.0768) 1 August 1999 (213) 1606:22.005 UT

Moment, dyn cm	Depth, km	Strike, deg	Dip, deg	Rake, deg	Source
7.00×10^{24} ($5.9M_w$)	8	216/39	45/45	−92/−88	SWPA[a]
3.60×10^{24} ($5.7M_w$)	8	226/39	64/26	−87/−96	TDMT[b]
1.82×10^{24} ($5.44M_w$)	8	194/71	64/42	−124/−41	GS[c]
3.60×10^{24} ($5.7M_w$)	8	190	52 to 45	−120 to −125	this study[d]

[a]Surface wave phase analysis, University of California, Berkeley.
[b]Time domain moment tensor, University of California, Berkeley.
[c]Grid search, California Institute of Technology.
[d]Fault parameters represent a range of values.

[16] After defining the source parameters for both earthquakes, we group similar waveform data into swaths, numbered 1–4 in Figure 5. We define "similar data" as data without dramatic changes in relative amplitude and without polarity reversals within the swath. Swaths 1 and 2 provide the primary waveform data used in deriving the velocity model. Swaths 3 and 4 will only provide confirmation of the model as both intersect a nodal plane, making their source parameter estimates unstable and modeling results less meaningful. Representative vertical velocity waveforms from swaths 1 and 2 are plotted in Figure 3b and compared to a synthetic from a 1-D model. Recordings from swath 1, labeled "typical" in Figure 3b, with corresponding path along the eastern edge of Death Valley, are similar to the 1-D waveforms and will be discussed first. Recordings from swath 2, "atypical" in Figure 3b, which traverse the southern Sierra Nevada are complex and will be discussed later.

3.2.1. Swath 1

[17] Displacement and velocity waveform data for swath 1 from the earthquake near the California-Nevada border are plotted in Figure 6. In the displacement data, two clear arrivals are present, *Pn* and *sPn*, shown in shaded boxes. On some records, *pPn* arrives between *Pn* and *sPn* but is much smaller in amplitude. A strong reflected arrival off the Moho, *PmP*, is also present and its onset is indicated by a line. All *Pn* phases travel along and beneath the Moho and appear step-like in displacement (Figure 6, top). The radial component *Pn*, not shown, has a similar wave shape, indicating that the velocity structure near the receiver is simple. It is difficult to describe the full range of models which can explain the data due to the nonuniqueness of waveform modeling. However, specific features of the waveforms, such as *Pn* width and *PmP* arrival times, are sensitive to small perturbations in the velocity model and can be used to highlight which portions of the velocity model are believable.

[18] We model these data in a forward sense with a simple layered model, eastern Mojave (Table 3). This model is derived from the Mojave model [*Jones and Helmberger*, 1998]. Synthetic waveforms, shown to the right of the data, are computed by frequency-wave number (FK) integration [*Saikia*, 1994] convolved with a triangle source (half width of 1 s). The velocity and thicknesses of the top layers were changed to achieve a better fit to the timing and amplitude of *Pn* and *PmP* at <200 km distance. Similar to the Mojave model, the midcrust of the eastern Mojave model is a single velocity layer. The data in Figure 6 do not show arrivals resulting from a reflector in the midcrust so a Conrad or midcrustal discontinuity is not included in the 1-D model. The velocity transition from the lower crust to the mantle is gradual in the eastern Mojave model. A sharp transition from the lower crust to the mantle would produces an impulsive *Pn*, which is not desired. A smooth lower crust to mantle transition renders the *Pn* to be dispersed so that its waveforms are relatively broad, desirable for both *Pn* and *PmP*. A velocity gradient structure in the mantle similar to the tectonic North America (TNA) model [*Grand and Helmberger*, 1984] had no effect on the waveforms and can therefore be constrained. The travel times of *Pn* and *sPn* increase linearly with distance, implying that we do not need to invoke complex velocity structure, such as discontinuities.

[19] Next, we compare velocity data with synthetics to demonstrate that the velocity model does not explain higher-frequency signals in *Pn* and *sPn*. A much larger time window for the displacement waveforms is used which includes the impulsive arrival *PmP*. The smaller time window for the velocity data only shows *Pn* and *sPn*, and not *PmP*. The use of velocity data allows us to resolve fine-scale structure, <5 km vertically, whereas displacement data resolve only larger-scale features. The velocity waveforms show more complexity than found in the synthetics. The *Pn* waveform is either wider or is composed of two arrivals at stations SAL and BC3, while larger than expected arrivals between *Pn* and *sPn* are recorded at stations DAN, SWS, and BTC. *Pn* arrivals recorded at these stations might be near the boundary between a simple 1-D type structure and a 2-D velocity structure to the west.

3.2.2. Swath 2

[20] A record section of vertical velocity waveforms from the Mammoth Lakes earthquake, for a swath that traverses the southern Sierra Nevada, is shown in Figure 7 (swath 2 in Figure 5). The radial (not shown) and vertical components are similar in appearance, indicating that the velocity structure near the receiver is simple. The consistency of the *Pn* wave shape across the entire swath also suggests a simple crustal velocity structure near the receivers. *Pn* propagating through the southern Sierra Nevada upper mantle include an anomalous arrival, which we label as Pn', that follows the initial *Pn*. *Pn* is the first positive pulse and marked by the left gray box, while Pn' is a combination of the next positive and negative pulse and marked with the right gray box. We assign the arrival a name Pn' as it arrives coincident with *Pn* and is also derived from the *Pn* wave field, discussed later. Pn' arrives 0.75–1.0 s after *Pn* but with a similar slowness so that it propagates a similar path. We examine models of crustal and mantle roots that have been proposed by previous investigators in an attempt to explain the origin of Pn'.

[21] In sections 3.2.2.1 and 3.2.2.2, we will focus on the *Pn* waveforms and only show *PmP* at smaller distances. By analyzing only the *Pn* arrivals we constrain only the crust-mantle interface and the mantle below. We use a simple layered model for the mid to upper crust which is unconstrained by the *Pn* waveforms. Synthetics are computed using a 2-D finite difference technique from *Helmberger and Vidale* [1988] with a source depth of 8 km and a triangular half width of 1 s. As with swath 1, we use a forward modeling approach to explain the data. We cannot adequately assess the full family of models which might describe the data, but by addressing features in the data which are reproducible through synthetics we can specify which parts of the model the data are sensitive to. The technique used here is not sensitive to fine-scale (<10 km) structure because the sources we use are earthquakes with source lengths close to 1 s. A comparison of synthetics from sections 3.2.2.1 and 3.2.2.2 is included later to highlight the major differences between a thick crustal root and a slow velocity mantle.

3.2.2.1. Crustal Root

[22] In this section we analyze how a crustal root affects *Pn* as they travel along the Sierra Nevada. We use three models with crustal thicknesses that vary from 40, 50, to 60 km, according to the north-south profile of *Pakiser and*

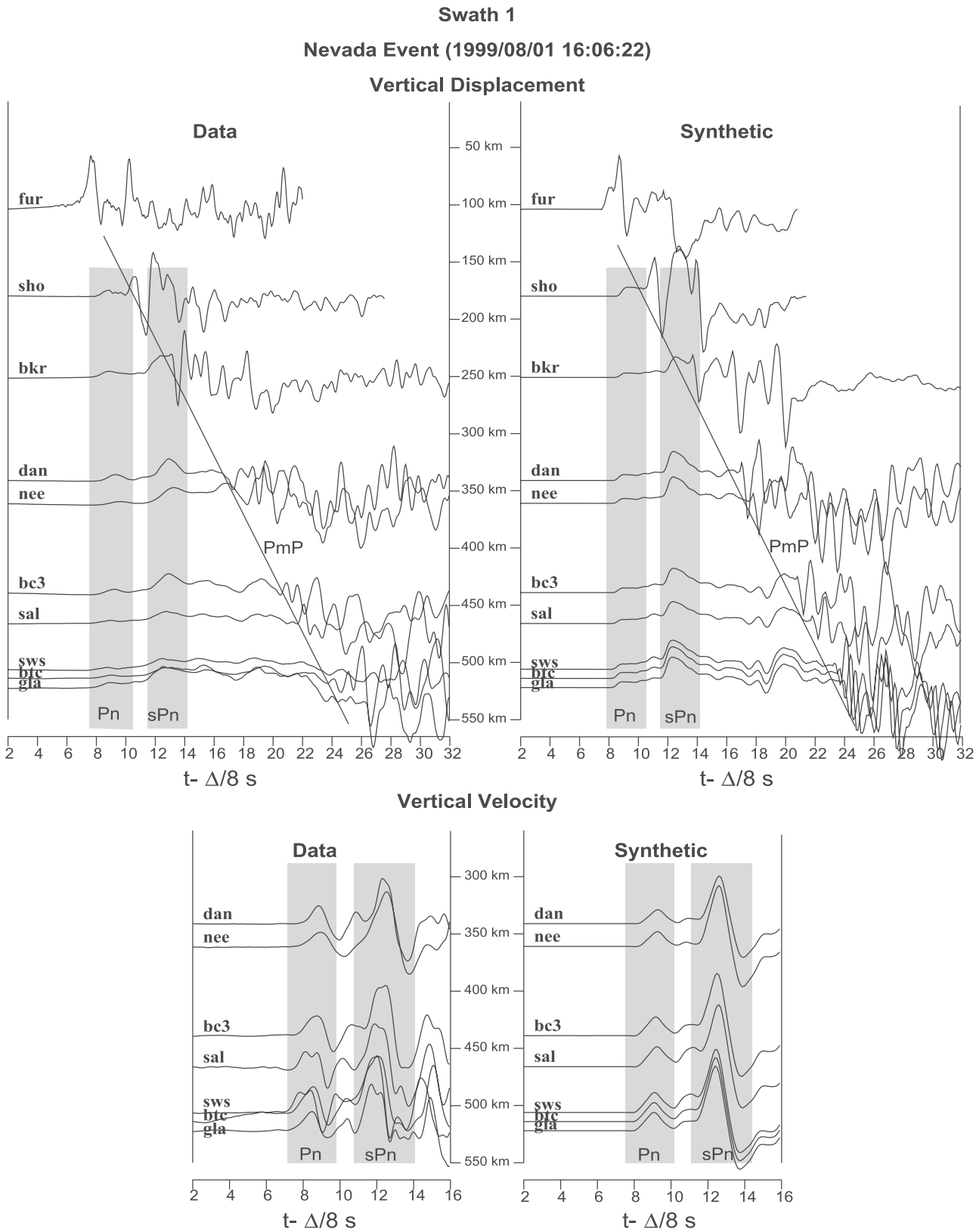

Figure 6. Comparison between data (displacement and velocity) and associated synthetics for swath 1 in Figure 5. Arrivals *Pn* and *sPn* are highlighted in gray boxes and the approximate arrival time for *PmP* is indicated by a line. The velocity model which produced the synthetics is displayed in Table 3. A vast majority of the data are explained by this simple flat-layered model.

Table 3. Swath 1 Eastern Mojave Velocity Model

Thickness, km	V_p, km/s	V_s, km/s	Density, kg/m^3
4	5.0	2.9	2400
19	6.1	3.5	2800
5	6.8	3.8	2800
2	7.0	4.0	2900
2	7.5	4.2	3000
Half-space	8.05	4.42	3200

Brune [1980] (Figures 8a, 8b, and 8c). The north-south profile from *Pakiser and Brune* [1980] was scaled to create crustal roots of differing depths and to assess how well a crustal root model explains the data in swath 2. Each crustal root model produces two distinct arrivals, *Pn* and *sPn* (gray boxes), for a given crustal thickness (Figure 9). The crustal thickness only affects the absolute timing of *Pn* and *sPn*, with thicker crustal roots producing a larger travel time delay in the arrival of each *Pn* phase. The main flaw of all of these model synthetics is that they do not include the large arrival, *Pn′*, seen in the data with its associated negative pulse. For a crustal thickness of 50 km the *Pn* arrival appears trapezoidal, not triangular as for crustal thicknesses of 40 and 60 km. The trapezoidal shape results from *Pn* interfering with reverberations in the crust. However, this second arrival from the 50 km crustal root does not contain a downswing, as in the data.

3.2.2.2. Low-Velocity Mantle

[23] As an alternative to the crustal root models, we examine the effects on regional waveforms using models with a lower velocity mantle structure. As shown before in Figure 3, a simple 1-D crustal model over a half-space mantle will produce simple arrivals. We can predict the *Pn* travel time variation by splitting the mantle into slow and fast regions, but we cannot reproduce the second arrival, *Pn′*. The second arrival, *Pn′*, appears to be a reflection not a refraction. Refraction arrivals, like *Pn*, appear triangular-like in velocity, while postcritical reflections are double-sided, a positive triangular pulse followed by a negative triangular pulse, like *Pn′*. If we add a slow velocity near the source (left side of Figure 8d) with a discontinuity at its base, we can reproduce the second arrival, *Pn′*. Since the discontinuity is deep, it does not affect *Pn*. A wave with a slightly different ray path will reflect off this boundary and, subsequently, follow a path similar to *Pn*. Figures 8d and 8e show two models producing a second arrival, *Pn′*. The arrival times of *Pn* and *Pn′* in Figure 10 are controlled by the velocity and the depth of the anomaly. The model in Figure 8d has a velocity of 7.6 km/s and a base at a depth of 75 km. A velocity of 7.6 km/s is similar to that reported by *Carder* [1973] and *Zhao* [1993]. The second arrival, *Pn′*, is the reflection off the discontinuity but is still a part of the *Pn* wave field. An anomaly with a flat bottom (Figure 8d) produces arrivals *Pn* and *Pn′* which intersect each other at ~400 km epicentral distance (Figure 10a). The different shading in Figure 10a shows how *Pn* intersects with *Pn′* to produce one arrival. At distances less than 350 km *Pn′* travels much slower than *Pn*, as it must travel to the discontinuity and back entirely within the anomaly. At distances greater than 350 km the reflection travels in the mantle just below the Moho, similar to a refraction in speed but arrives double-sided in shape. By dipping the discontinuity away from the source (Figure 8e), the arrival of *Pn′* at larger distances does not interfere with *Pn* (Figure 10b) instead producing two distinct arrivals. On the basis of these observations, Figure 8e is our preferred model. The low velocity, 7.6 km/s, explains the travel times of *Pn* and a 10°–15° south dipping discontinuity with the depth in the north at ~75 km and ~100 km in the south produces two arrivals 0.75–1.0 s apart for over 300 km in distance.

[24] The low-velocity zone in our preferred model is well resolved except on the source side. The low-velocity zone in the mantle is immediately below the crust, constrained by waveform modeling. The depth of the discontinuity is

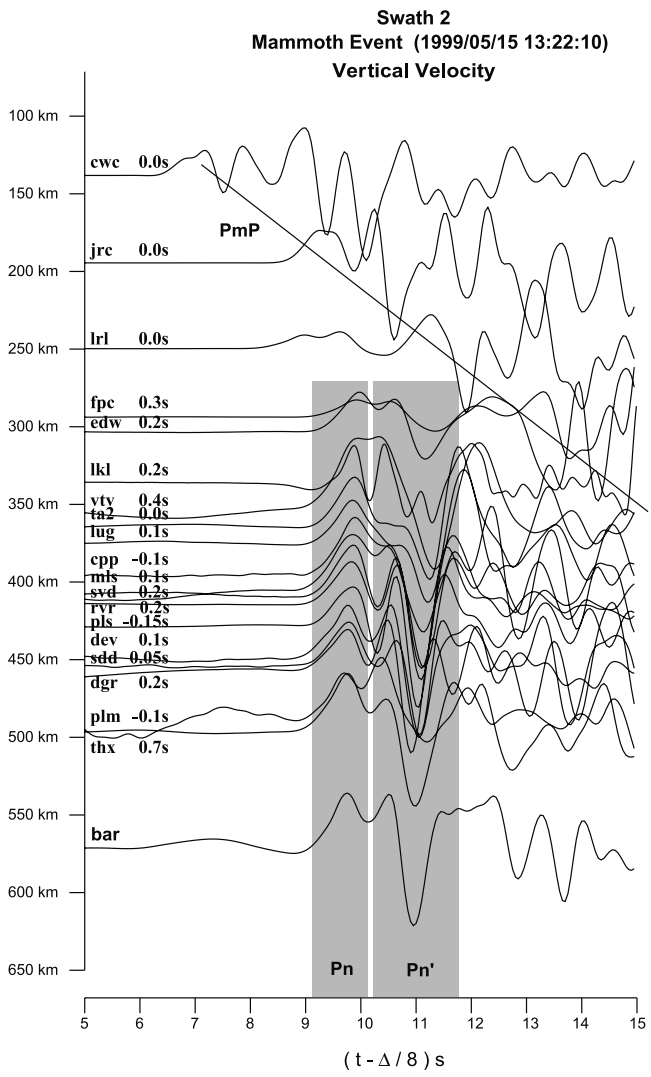

Figure 7. Record section from swath 2 showing waveform data traversing the southern Sierra Nevada (Figure 5). Notice two arrivals *Pn* and *Pn′*, indicated by gray boxes, arriving less than 1 s apart and the large downswing associated with the later *Pn′* arrival. The data are reduced using a velocity of 8.0 km/s. Time shift required to align *Pn* is shown after the station name; a positive shift moves the trace to the right. Synthetics for crustal and mantle anomalies are computed to explain the shape and timing of the *Pn* arrivals.

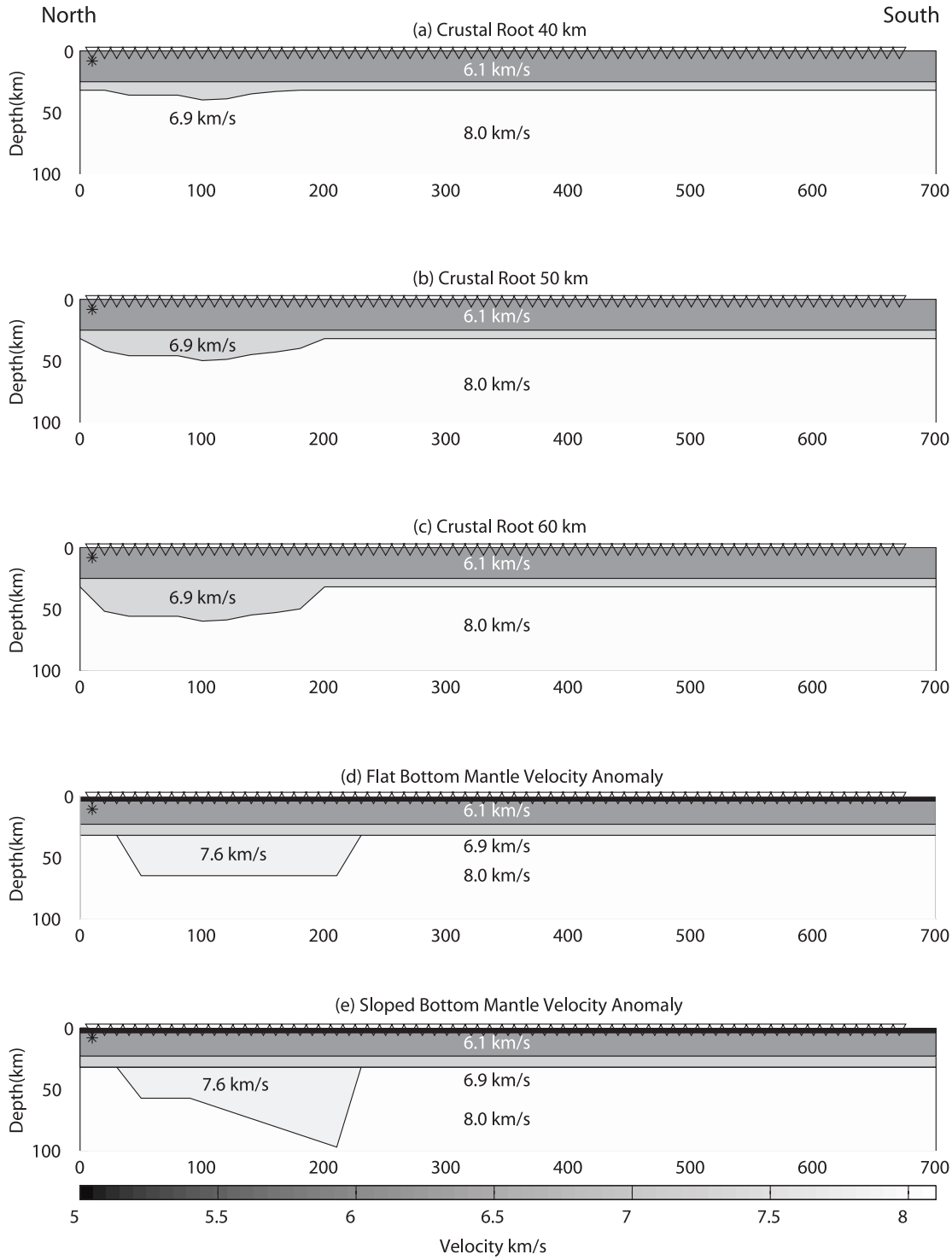

Figure 8. (a, b, c) Three models of crustal roots derived from *Pakiser and Brune* [1980] to explain the arrival times from the 1966 Truckee Earthquake. The maximum crustal thicknesses are 40 (Figure 8a), 50 (Figure 8b) and 60 km (Figure 8c), while the crustal thickness near the receiver is 32 km. A discontinuity at 25 km separates the 6.1 km/s upper crust from the 6.9 km/s lower crust and root. (d) Velocity model with a flat bottomed anomaly, 7.6 km/s, just below the crust extending down to 75 km. (e) Refinement of the model in Figure 8d by addition of a sloped bottom to align *Pn* and *Pn′*. This refinement puts the maximum depth at 100 km. Lighter shades are faster velocities. All models have sources, stars, in the north, left edge, and the waves propagate to the south, right edge.

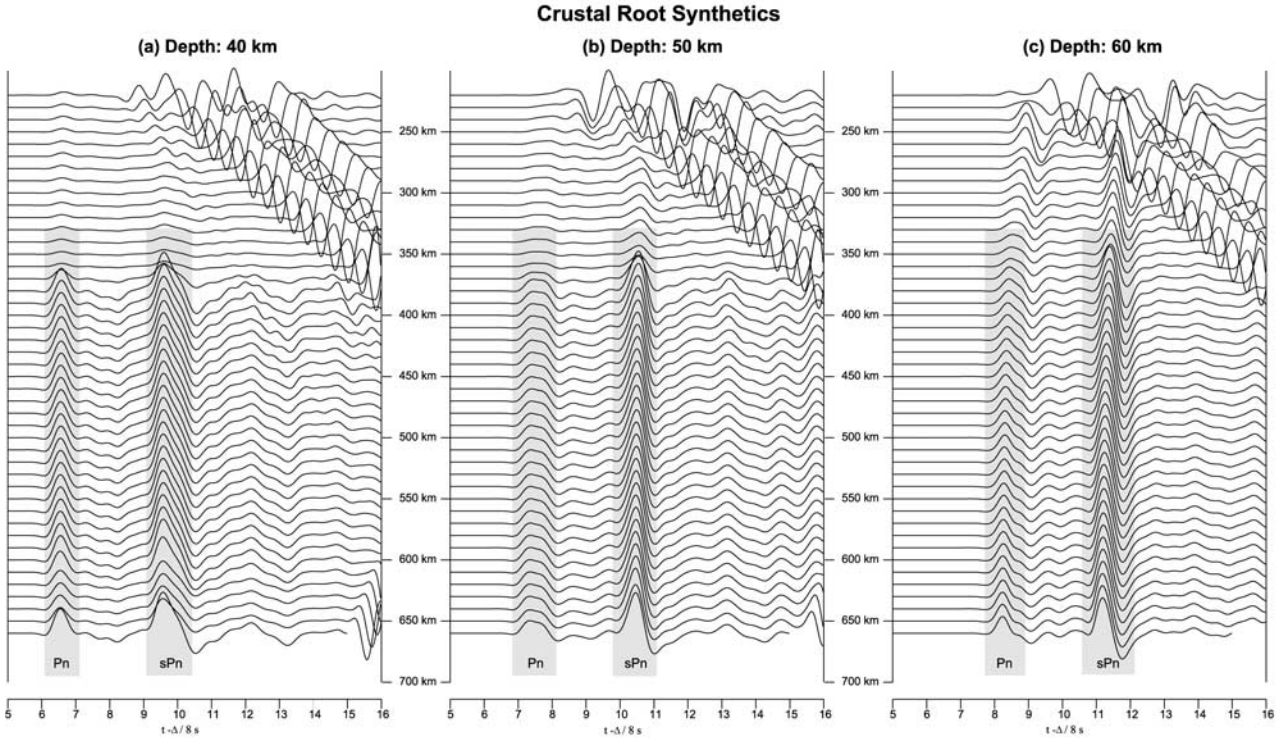

Figure 9. Synthetics for the three crustal root models derived from *Pakiser and Brune* [1980] and shown in Figures 8a, 8b, and 8c. Note that only the 50 km crustal root model shows two arrivals for *Pn*, forming a trapezoidal shape, but it lacks the large downswing associated with second arrival, *Pn′*, which is present in the data (Figure 7). *Pn* and *sPn* are highlighted in the gray boxes.

proportional to the relative travel time of *Pn′* with respect to *Pn*. A deeper discontinuity produces larger time delays between *Pn* and *Pn′*, while a shallow discontinuity reduces the relative travel time between *Pn* and *Pn′*. However, the depth of the discontinuity does trade off with V_p in the low-velocity zone. If the discontinuity is replaced with a gradient, the *Pn′* arrival becomes longer period and lower in amplitude. The *Pn′* arrival is impulsive with a large amplitude; from this we conclude the boundary is nearly a discontinuity. The same discontinuity at >150 km depth does not produce the *Pn′* arrival. By using the relative amplitude and timing of these phases we can constrain the southern boundary of the low-velocity zone. However, dramatic changes in the *Pn* wave field do occur between stations VTV and TA2, indicating that this structure that we explain with a simple 2-D model is more complicated than modeled here. Shifting the entire low-velocity zone to the left, or north, by 10 km increases the relative amplitude of *Pn* with respect to *Pn′*, and the time separation between *Pn* and *Pn′* also increases. As the low-velocity zone is shifted south, the relative amplitude of *Pn* decreases as does the relative travel time between *Pn* and *Pn′*. The same effect occurs by only shifting the southern boundary. In contrast, by only shifting the left or northern boundary, the waveform shapes and travel times do not change appreciably. This indicates that we are not sensitive to the northern extent of the slow velocity region but can constrain the southern boundary to within ~10 km. The poor sensitivity in the north results from *Pn* entering the low-velocity zone from the top and never sampling the northernmost portion of our study area. The southern boundary, coincident with the surface trace of the Garlock Fault, is well sampled by the *Pn* waveforms studied in swath 2.

3.2.2.3. Model Comparison

[25] Velocity waveform data from station PLM at a distance of 500 km are plotted (Figure 11) against synthetics from a layer over a half-space (1-D), a 50 km crustal thickness model (Figure 8b), and our preferred model (Figure 8e). The 1-D model fails to explain the anomalous second arrival, *Pn′*. The 50 km crustal thickness model produces complex *Pn* behavior. The thicker crust produces a second arrival which makes *Pn* appear trapezoidal in shape. The second arrival, while consistently trailing *Pn* by 0.5–1.0 s, is not double-sided, as seen in the data. Our preferred model, with a discontinuity at 75–100 km beneath a low-velocity mantle, produces an second arrival, *Pn′*, similar to the double-sided arrival in the data. The reflection creates a double-sided arrival in velocity, thus producing a large downswing.

3.2.3. Swath 3

[26] Vertical velocity data from swath 3 (Figure 5) are plotted in Figure 12. This swath begins in Mammoth and trends toward the Mojave desert. The two arrivals, marked as *Pn* and *Pn′*, are less than a second apart, and there are no additional signals until the arrival of the reflection from the Moho, *PmP*. The relative timing between *Pn* and *Pn′* is similar to that seen on the southern Sierra Nevada profile. Modeling this swath with the preferred model (Figure 8e)

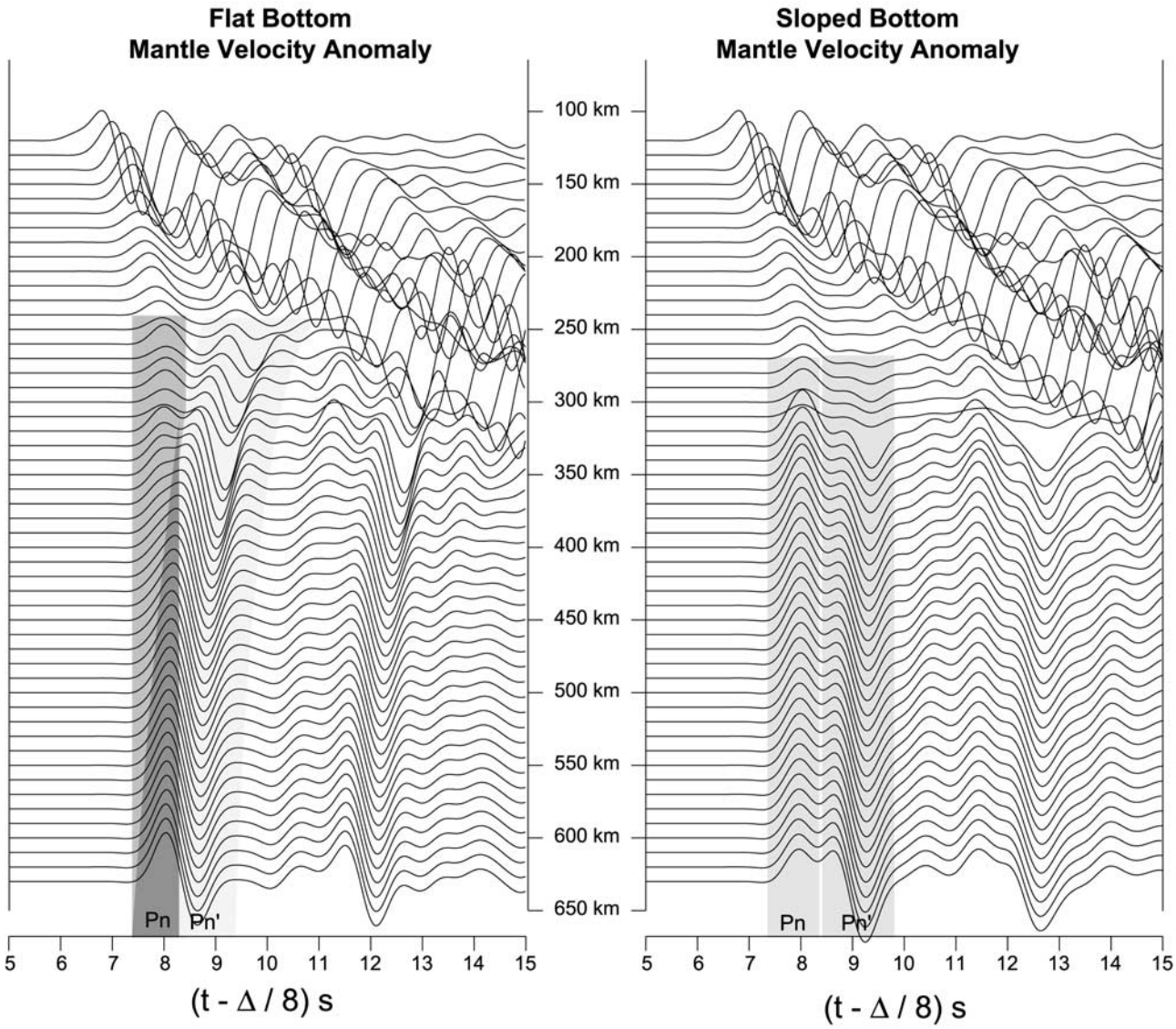

Figure 10. Synthetics for the two mantle velocity anomalies shown in Figures 8d and 8e. (left) Flat bottomed anomaly. It produces two arrivals, a single-sided *Pn* (dark gray box), and a double-sided *Pn′* (light gray box), similar to the data in Figure 7, but at large distances the arrivals converge (intermediate gray area). (right) Sloped bottom anomaly. If the bottom of the anomaly is sloped away from the source, as shown in Figure 8e, then *Pn* and *Pn′* do not intersect but maintain a consistent travel time difference, in accordance with the data (two independent gray boxes).

produces the arrivals *Pn* and *Pn′* with relative timing and amplitude similar to that found in the data. The depth phase, *sPn*, exhibits amplitude differences between the data and synthetics due to the source mechanism as *sPn* approaches a node at this azimuth. However, trying to predict amplitudes near a source mechanism node is difficult because small changes in the source mechanism can create large changes in amplitudes. Waveforms data from this swath show that the preferred model also explains the double-sided pulse, *Pn′*, for paths which traverse the southern Walker Lane extending out to Death Valley.

3.2.4. Swath 4

[27] Swath 4 (Figure 5) contains the complementary crossing swath from the Nevada earthquake, and we plot its record section in Figure 13. This swath occurs near a amplitude node for *Pn* and exhibits small amplitudes in comparison to the swaths discussed previously. Perturbations in the source mechanism of 20° in rake dramatically change the amplitudes of the arrivals at this azimuth (∼190°). With a nodal *Pn* the first arrival is *Pn′*, and the second and third are *pPn* and *sPn* (marked in Figure 13). A simple 1-D model, as used for data farther to the east, only produces three isolated pulses, which do not match the complex waveforms for this swath of data. However, use of the velocity structure of our preferred model produces the extra arrivals needed to match the data, marked as *Pn′*, *pPn′*, and *sPn′* in Figure 13. Again, near-nodal arrivals complicate the resulting waveforms. Energy arriving near a node is

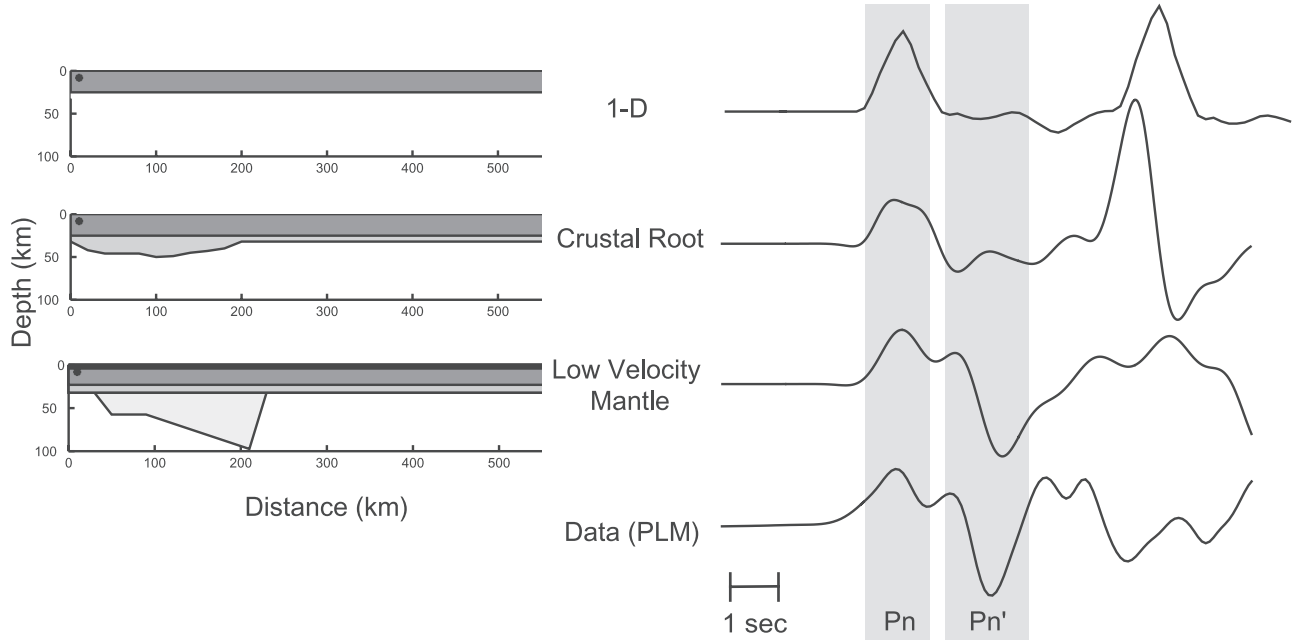

Figure 11. Comparison of three velocity models and associated *Pn* waveforms with data recorded at station PLM (Palomar, California) from swath 2. (top) The model of a layer over a half-space similar to Figure 3 and synthetic *Pn* waveform. (middle) The 50 km thick crustal model of Figure 8b. (bottom) The preferred model of Figure 8e. All waveforms are vertical velocity data at 500 km epicentral distance. Notice the large downswing of *Pn′* in the data and mantle velocity anomaly synthetic, which is absent in the crustal model and layer over a half-space.

weakly coherent and could appear shifted in time due to velocity perturbations. Nevertheless, coherent arrivals at distances >325 km are apparent and marked in gray boxes in Figure 13. Our preferred velocity model explains seismic wave propagation through the southern Sierra Nevada and Walker Lane.

4. Gravity

[28] The densities in the preferred model can be reconciled with gravity observations. Modeling of gravity data in a east-west profile across the Sierra Nevada and Basin and Range by *Fliedner and Ruppert* [1996] places density variations within the upper mantle rather than the crust. While the same gravity data can also be explained by using only crustal density variations, *Fliedner and Ruppert* [1996] state that the overall crustal density would then deviate from a reasonable crustal average. Converting the low mantle velocities of the preferred model (Figure 8e) into densities, as accomplished by *Schmitz et al.* [1997], renders variations of $\sim$60–140 kg/m^3 [*Fliedner and Ruppert*, 1996] between the surrounding mantle and the low-velocity region. Using a density variation of 80 kg/m^3 at depths from 35 to 75 (or 100) km produces an Bouguer gravity anomaly of ~ -100 (or -140) mGal. An anomaly of -100 mGal in Walker Lane is therefore explainable by either the modeling of *Fliedner and Ruppert* [1996] or our preferred model. While our preferred model may overestimate the gravity anomaly, partial melt in small percentages reduces the Bouguer gravity magnitude [*Schmitz et al.*, 1997] to less than -100 mGal. Our preferred model agrees with the Bouguer gravity if we assume a velocity-density relation with a possibility of partial melt in the upper mantle.

5. Conclusions

[29] A low-velocity V_p 7.6 km/s anomaly is present underneath the Sierra Nevada and Walker Lane. There is also a large velocity discontinuity at $\sim$75–100 km depth, dipping southward at 10–15°. A thick crustal root does not explain the Mammoth Lake earthquake waveform data along the Sierra Nevada axis (swath 2) due to the lack of an double-sided arrival following *Pn* (Figure 11). The western edge of the low-velocity zone is beneath the Sierra Nevada and extends to the east beneath Death Valley. The southern extent does not cross the Garlock fault but becomes deeper while approaching this boundary. The eastern edge of this anomaly does not extend past Death Valley. From the modeling of recordings from swath 1, a simple flat-layered velocity structure (Table 3) is suggested for the eastern Mojave and east of Death Valley. Data from swath 2 show behavior similar to that for swaths 3–4, with a prominent secondary arrival, *Pn′*. Our results compare well with those of *Carder et al.* [1970], *Carder* [1973], *Savage et al.* [1994], and *Fliedner et al.* [2000]. The absence of a high-velocity lower lithosphere in our model compares well with the tomography studies of *York and Helmberger* [1973], *Biasi and Humphreys* [1992], *Zhao* [1993], and *Pollitz* [1999] that indicate a low-velocity mantle beneath the southern Sierra Nevada. The structural components above are compatible with models from *Wernicke et al.* [1996] and *Jones and Phinney* [1998], but the large velocity discontinuity at 75–100 km is a new model feature.

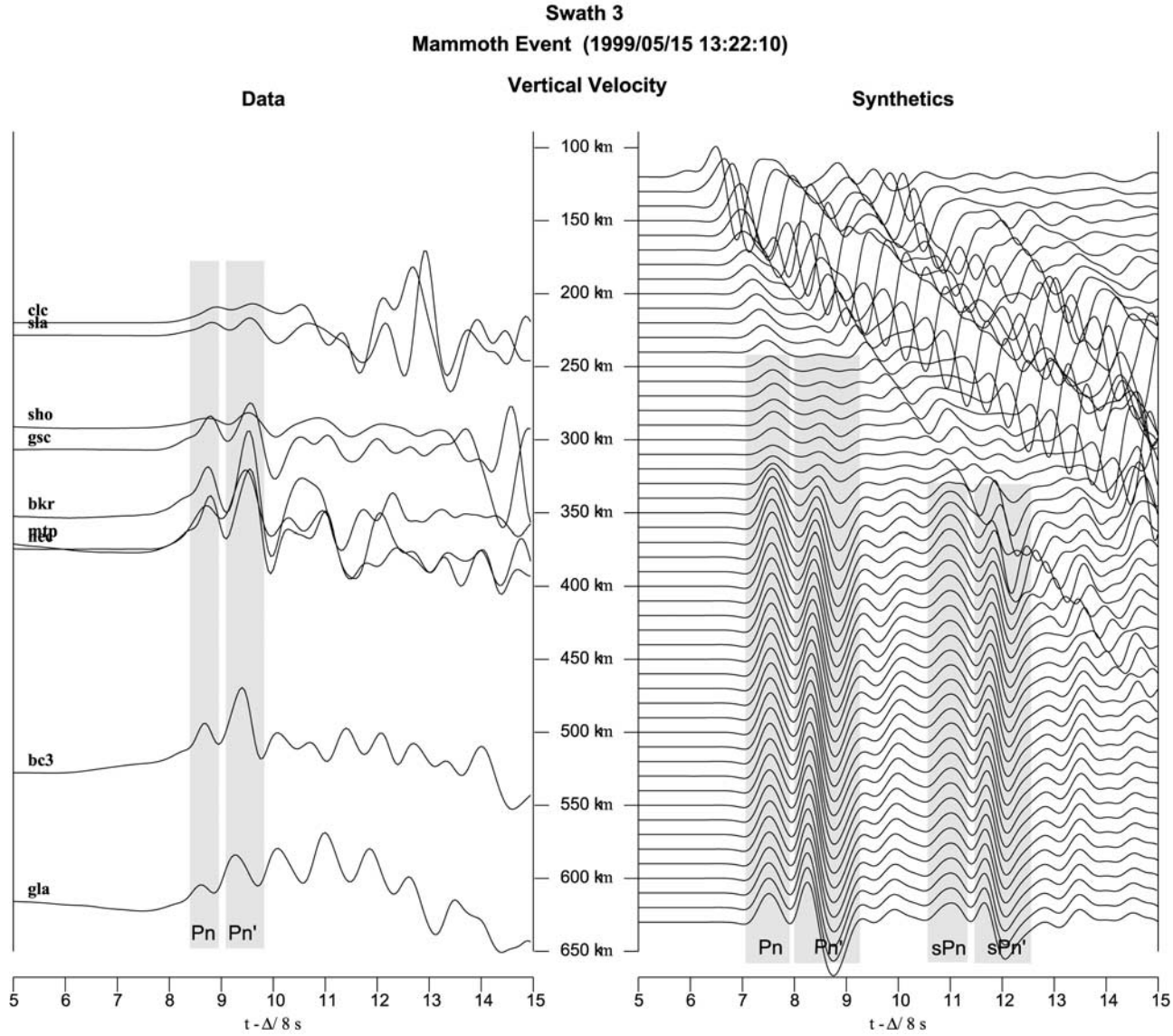

Figure 12. Velocity data and synthetics for the southeastern crossing swath for the Mammoth event, swath 3 in Figure 5. The low amplitude of *sPn* relative to *Pn* in the data and synthetics is due to *sPn* being near nodal for this azimuth. Notice the large downswing associated with *Pn′* at stations near 350 km. This is similar to data seen in swath 2 and synthetics computed for Figure 8e.

[30] Integrating our inference of a large-scale discontinuity at depth (75–100 km) and previously reported low-velocity mantle below the southern Sierra Nevada and Walker Lane [*Carder et al.*, 1970; *Carder*, 1973; *Biasi and Humphreys*, 1992; *Zhao*, 1993; *Savage et al.*, 1994; *Fliedner et al.*, 2000] in a tectonic framework is complex. Development of the Sierra Nevada and its underlying mantle lithosphere initially occurred during subduction between the North American and Farallon plates. Subduction along the western North American border continued with varying degrees of slab dip until 28–19 Ma. At that point in time, a slab window, or slab gap, marking the end of subduction began to form. As the slab window grew larger and migrated northward, the oceanic lithosphere sank and left hot asthenosphere in contact with the upper crust to the west of the Sierra Nevada. Development of a slab window and cooling asthenosphere produces convective instabilities which form drip-like structures in the upper mantle [*Zandt and Carrigan*, 1993; *Houseman et al.*, 2000]. At 8–6 Ma the lithosphere of the Sierra Nevadas disappears [*Ducea and Saleeby*, 1998c], leaving hot asthenosphere below the Sierra Nevada. At approximately the same time, ~8 Ma, the relative motion of the Pacific plate to North America rotated to a more northern direction.

[31] Verifying the existence and location of the subducted slab (Farallon plate), a possible drip-like structure, and location of a missing mantle lithosphere is useful in constraining tectonic and dynamic convection models. First, the subducted slab is likely underlying the northern Sierra due to a component of northern velocity during subduction. Second, the drip-like structure is reportedly seen tomographically [*Biasi and Humphreys*, 1992] as a

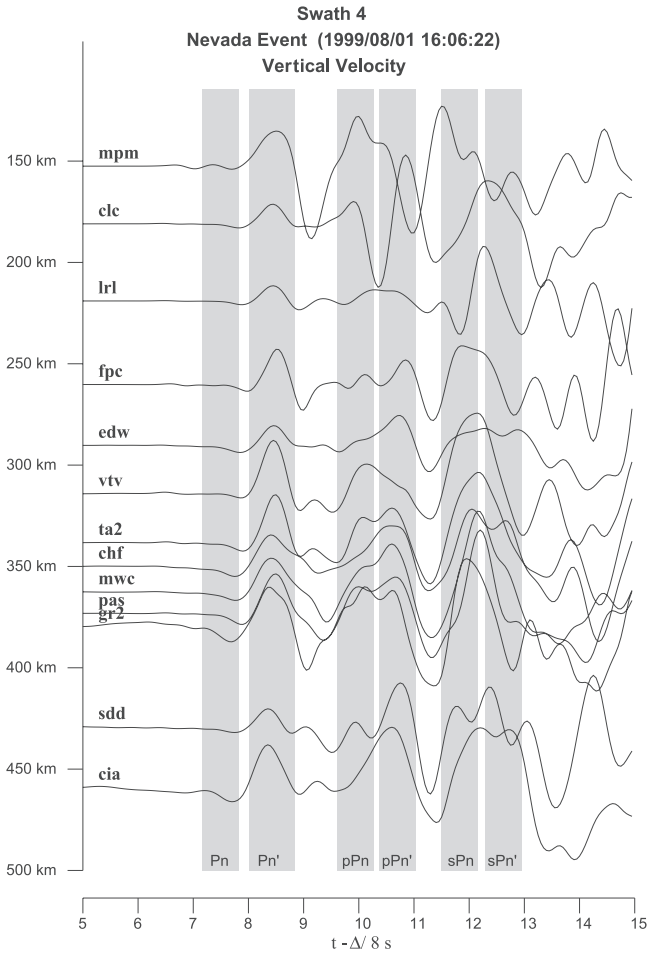

Figure 13. Data from the Nevada event which propagates southwest, swath 4 in Figure 5. These data are explained by the preferred model, Figure 8e, but full waveform modeling becomes difficult as the data are near nodal. However, double arrivals are present for *Pn*, *pPn*, and *sPn*, as for swaths 2 and 3, especially at larger distances, >325 km. Gray boxes are used to identify approximate arrival times of *Pn*, *pPn*, and *sPn* as the wave shape may appear to perturb arrival times near a node.

cylindrical high-velocity structure at 150–200 km depth called the Southern Great Valley Anomaly. Several mechanisms could be responsible for the disappearance of the Sierra Nevada mantle lithosphere. Either the lithosphere detached from the upper crust above it and sunk into the surrounding mantle or the lithosphere was chemically incorporated into the mantle. Our results show a discontinuity at depth and thus support the sinking lithosphere hypothesis. We hypothesize the discontinuity as the old contact between the Sierra Nevada lithosphere and crust. Moreover, mantle flow resulting from a sinking lithosphere will fill the area left by the sinking lithosphere from the neighboring sides and below. If the flow originates from the hotter asthenosphere below, then it could be the mechanism that places lower-velocity, hotter mantle at the base of the crust. Dynamic models with realistic density and viscosity variations are necessary to accurately test if these structures are viable.

[32] **Acknowledgments.** We would like to thank Jascha Polet, Hiroo Kanamori, Egill Hauksson, Matt Pritchard, Jeroen Ritsema, and Mark Simons as well as two anonymous reviewers for their reviews. We would also like to thank Alisa Miller, Pete Savage, Nathan Niemi, Rowena Lohman, and Jason Saleeby for their helpful discussions, and TriNet and Berkeley Digital Seismological Network (BDSN) for seismic waveform data. This research was supported by the Defense Threat Reduction Agency under contract DSWA01-98-1-0010. Contribution 8827, Division of Geological and Planetary Sciences, California Institute of Technology, Pasadena, California.

References

Atwater, T., and J. Stock, Pacific North America plate tectonics of the Neogene southwestern United States: An update, *Int. Geol. Rev.*, *40*, 375–402, 1998.

Bailey, R. A., G. B. Dalrymple, and M. A. Lanphere, Volcanism, structure, and geochronology of Long Valley Caldera, Mono County, California, *J. Geophys. Res.*, *81*, 725–744, 1976.

Bateman, P. C., and J. P. Eaton, Sierra Nevada Batholith, *Science*, *158*, 1407–1417, 1967.

Biasi, G., and E. Humphreys, *P*-wave image of the upper mantle structure of central California and southern Nevada, *Geophys. Res. Lett.*, *19*, 1161–1164, 1992.

Burchfiel, B. C., D. S. Cowan, and G. A. Davis, Tectonic overview for the Cordilleran orogen in the western United States, in *The Geology of North America*, vol. G3, *The Cordilleran Orogen: Conterminous U.S.*, edited by B. C. Burchfiel, P. W. Lipman, and M. L. Zoback, pp. 1–7, Geol. Soc. of Am., Boulder, Colo., 1992a.

Burchfiel, B. C., P. W. Lipman, and M. L. Zoback, Introduction, in *The Geology of North America*, vol. G-3 *The Cordilleran Orogen: Conterminous U.S.*, edited by B. C. Burchfiel, P. W. Lipman, and M. L. Zoback, pp. 407–479, Geol. Soc. of Am., Boulder, Colo., 1992b.

Byerly, P., Comment on "The Sierra Nevada in the light of isostasy," *Bull. Geol. Soc. Am.*, *48*, 2025–2031, 1937.

Carder, D. S., Trans-California seismic profile, Death Valley to Monterey Bay, *Bull. Seismol. Soc. Am.*, *63*, 571–586, 1973.

Carder, D. S., A. Qamar, and T. V. McEvilly, Trans-California seismic profile-Pahute Mesa to San Francisco Bay, *Bull. Seismol. Soc. Am.*, *60*, 1829–1846, 1970.

Chase, C. G., and T. C. Wallace, Flexural isostasy and uplift of the Sierra Nevada of California, *J. Geophys. Res.*, *93*, 2795–2802, 1988.

Crough, S. T., and G. A. Thompson, Upper mantle origin of Sierra Nevada uplift, *Geology*, *5*, 396–399, 1977.

Ding, X., and D. V. Helmberger, Modelling D″ structure beneath Central America with broadband seismic data, *Phys. Earth Planet. Inter.*, *101*, 245–270, 1997.

Ducea, M. N., and J. B. Saleeby, Buoyancy sources for a large, unrooted mountain range, the Sierra Nevada, California: Evidence from xenolith thermobarometry, *J. Geophys. Res.*, *101*, 8229–8244, 1996.

Ducea, M. N., and J. B. Saleeby, Crustal recycling beneath continental arcs: Silica-rich glass inclusions in ultramafic xenoliths from the Sierra Nevada, California, *Earth Planet. Sci. Lett.*, *156*, 101–116, 1998a.

Ducea, M. N., and J. B. Saleeby, The age and origin of a thick mafic-ultramafic keel from beneath the Sierra Nevada batholith, *Contrib. Mineral Petrol.*, *133*, 169–185, 1998b.

Ducea, M. N., and J. B. Saleeby, Case for delamination of the deep batholithic crust beneath the Sierra Nevada, California, in *Integrated Earth and Environment Evolution of the Southwestern United States: The Clarence A. Hall, Jr. volume, Papers from a symposim help Sept. 13–15, 1997 at the Crooked Creek Conference Center (Calif.)*, pp. 273–288, Bellwether, Columbia, Md., 1998c.

Dumitru, T. A., P. B. Gans, D. A. Foster, and E. L. Miller, Refrigeration of the western Cordilleran lithosphere during, *Geology*, *19*, 1145–1148, 1991.

Eaton, J. P., Crustal structure in northern and central California from seismic evidence, *Bull. Calif. Civ. Mines Geol.*, *190*, 419–426, 1966.

Fliedner, M. M., and S. Ruppert, Three-dimensional crustal structure of the southern Sierra Nevada from seismic fan profiles and gravity modeling, *Geology*, *24*, 367–370, 1996.

Fliedner, M., S. Klemperer, and N. Christensen, Three-dimensional seismic model of the Sierra Nevada arc, California, and its implications for crustal and upper mantle composition, *J. Geophys. Res.*, *105*, 10,899–10,921, 2000.

Grand, S. P., and D. V. Helmberger, Upper mantle shear structure of North America, *Geophys. J. R. Astron. Soc.*, *76*, 399–438, 1984.

Helmberger, D. V., and J. E. Vidale, Modeling strong motions produced by earthquakes with two-dimensional numerical codes, *Bull. Seismol. Soc. Am.*, *78*, 109–121, 1988.

Houseman, G., E. Neil, and M. Kohler, Lithospheric instability beneath the Transverse Ranges of California, *J. Geophys. Res.*, *105*, 16,237–16,250, 2000.

Jones, C. H., and R. A. Phinney, Seismic structure of the lithosphere from teleseismic converted arrivals observed at small arrays in the southern Sierra Nevada and vicinity, California, *J. Geophys. Res.*, *103*, 10,065–10,090, 1998.

Jones, C. H., H. Kanamori, and S. W. Roecker, Missing roots and mantle "drips": Regional Pn and teleseismic arrival times in the southern Sierra Nevada and vicinity, California, *J. Geophys. Res.*, *99*, 4567–4601, 1994.

Jones, L. E., and D. V. Helmberger, Earthquake source parameters and fault kinematics in the eastern California shear zone, *Bull. Seismo. Soc. Am.*, *88*, 1337–1352, 1998.

Lawson, A. C., The Sierra Nevada in the light of isostasy, *Geol. Soc. Am. Bull.*, *47*, 1691–1712, 1936.

Liu, M., and G. Zandt, Convective thermal instabilities in the wake of the migrating Mendocino triple junction, California, *Geophys. Res. Lett.*, *23*, 1573–1576, 1996.

Melbourne, T., and D. V. Helmberger, Mantle control of the plate boundary deformation, *Geophys. Res. Lett.*, *28*, 4003–4006, 2001.

Pakiser, L. C., and J. N. Brune, Seismic models of the root of the Sierra Nevada, *Science*, *210*, 1088–1094, 1980.

Pasyanos, M., D. Dreger, and B. Romanowicz, Toward real-time estimation of regional moment tensors, *Bull. Seismol. Soc. Am.*, *86*, 1255–1269, 1996.

Pollitz, F., Regional velocity structure in northern California from inversion of scattered seismic surface waves, *J. Geophys. Res.*, *104*, 15,043–15,072, 1999.

Saikia, C. K., Modified frequency-wave-number algorithm for regional seismograms using Filons quadrature-Modeling of *Lg* waves in eastern North America, *Geophys. J. Int.*, *118*, 142–158, 1994.

Saltus, R., and A. Lachenbruch, Thermal evolution of the Sierra Nevada: Tectonic implications of new heat flow data, *Tectonics*, *10*, 325–344, 1991.

Savage, M. K., L. Li, J. P. Eaton, C. H. Jones, and J. N. Brune, Earthquake refraction profiles of the root of the Sierra Nevada, *Tectonics*, *13*, 803–817, 1994.

Schmitz, M., W. Heinsohn, and F. Schilling, Seismic, gravity and petrological evidence for partial melt beneath the thickened central Andean crust (21–23 degrees s), *Tectonophysics*, *270*, 313–326, 1997.

Snow, J. K., and B. P. Wernicke, Cenozoic tectonism in the central Basin and Range: Magnitude, rate, and distribution of the upper crustal structure, *Am. J. Sci.*, *300*, 659–719, 2000.

Sonder, L. J., and C. H. Jones, Western United States extension: How the west was widened, *Annu. Rev. Earth Planet Sci.*, *27*, 417–462, 1999.

Weiland, C. M., L. K. Steck, P. B. Dawson, and V. A. Korneev, Nonlinear teleseismic tomography at Long Valley Caldera, using three-dimensional minimum travel time ray tracing, *J. Geophys. Res.*, *100*, 20,379–20,390, 1995.

Wernicke, B., Cenozoic extensional tectonics of the U.S. Cordillera, in *The Geology of North America*, vol. G3, *The Cordilleran Orogen: Conterminous U.S.*, edited by B. C. Burchfiel, P. W. Lipman, and M. L. Zoback, pp. 553–581, Geol. Soc. of Am., Boulder, Colo., 1992.

Wernicke, B., and J. K. Snow, Cenozoic tectonism in the central Great Basin and Range: Motion of the Sierran-Great Valley Block, *Int. Geol. Rev.*, *40*, 403–410, 1998.

Wernicke, B., et al., Origin of high mountains in the continents: The southern Sierra Nevada, *Science*, *271*, 190–193, 1996.

York, J. E., and D. V. Helmberger, Low-velocity zone variations in the southwestern United States, *J. Geophys. Res.*, *78*, 1883–1886, 1973.

Zandt, G., and C. Carrigan, Small-scale convective instability and upper-mantle viscosity under California, *Science*, *261*, 460–463, 1993.

Zhao, L. S., Lateral variations and azimuthal isotropy on *Pn* velocities beneath Basin and Range Province, *J. Geophys. Res.*, *98*, 22,109–22,122, 1993.

C. Ji, D. V. Helmberger, and B. Savage, Seismological Laboratory, Division of Geological and Planetary Sciences, Mail Code 252-21, California Institute of Technology, Pasadena, CA 91125, USA. (savage13@gps.caltech.edu)